

1 **How do gravity waves triggered by a typhoon propagate from the**
2 **troposphere to the upper atmosphere?**

3 Qinzeng Li¹, Jiyao Xu^{1,2}, Hanli Liu³, Xiao Liu⁴, Wei Yuan¹

4 ¹State Key Laboratory of Space Weather, National Space Science Center, Chinese Academy of
5 Sciences, Beijing, 100190, China,

6 ²School of Astronomy and Space Science, University of Chinese Academy of Science, Beijing,
7 100049, China,

8 ³High Altitude Observatory, National Center for Atmospheric Research, Boulder, CO
9 80307-3000, USA,

10 ⁴School of Mathematics and Information Science, Henan Normal University, Xinxiang, 453007,
11 China,

12

13 Correspondence to: xujy@nssc.ac.cn

14 **Abstract**

15 Gravity waves (GWs) strongly affect atmospheric dynamics, and photochemistry, as
16 well as the coupling between the troposphere, stratosphere, mesosphere, and thermosphere.
17 Also, GWs generated by strong disturbances in the troposphere (such as thunderstorms,
18 typhoons, etc.) can affect the atmosphere of the Earth ranging from the troposphere to the
19 thermosphere. However, the fundamental process of GW propagation from the troposphere
20 to the thermosphere is poorly understood because it is challenging to constrain this process
21 by observations. Moreover, GWs tend to dissipate rapidly in the thermosphere because the
22 molecular diffusion increases exponentially. In this study, a double-layer airglow network
23 is used to capture concentric gravity waves (CGWs) over China, which were excited by the
24 Super Typhoon Chaba (2016). We used the ERA-5 reanalysis data and Multi-functional
25 Transport Satellite-1 Observations and quantitatively described the physical mechanism of
26 typhoon-generated CGWs propagating throughout the stratosphere, mesosphere, and
27 thermosphere. We found that the CGWs in the mesopause region were generated directly by
28 the typhoon in the troposphere. However, like the relay, the backward ray tracing analysis
29 suggests that CGWs in the thermosphere originated from the secondary waves generated by
30 the dissipation of the CGW and/or nonlinear processes in the mesopause region .

31 **1. Introduction**

32 Gravity waves (GWs) can transfer momentum and energy from the lower to upper
33 atmospheres, thereby affecting the global circulation and thermal structures, as well as the
34 distribution of chemical composition in the middle and upper atmospheres (Holton, 1983;
35 Fritts and Alexander, 2003). The dynamic, photochemical, and electrodynamics processes
36 have indicated that GWs are fundamental for the coupling process between the troposphere,
37 stratosphere, mesosphere, and thermosphere (Liu and Vadas, 2013; Smith et al., 2013; Vadas
38 and Liu, 2013; Xu et al., 2015).

39 Concentric GWs (CGWs) are unique type of GWs that are considered to be mainly
40 generated by convective activity in the troposphere. CGWs can also be generated by primary
41 wave breaking (Vadas and Becker, 2019; Lund et al., 2020; Kogure et al., 2020) volcanoes
42 (Duncombe, 2022), nuclear explosions (Pfeffer and Zarichny, 1962; Pierce et al., 1971), and
43 rockets (Liu et al., 2020). CGWs in the stratosphere and mesosphere generated by
44 thunderstorms (Taylor and Hapgood, 1988; Sentman et al., 2003; Suzuki et al., 2007; Yue et
45 al., 2009; Xu et al., 2015; Heale et al., 2019; Smith et al., 2020) have been widely reported
46 since their sources are ubiquitous. In previous studies, CGWs induced by typhoons were
47 detected using ground-based optical remote sensing (Suzuki et al., 2013) while those
48 induced by hurricanes and tropical cyclones were detected using the Suomi National
49 Polar-orbiting Partnership satellite (Yue et al., 2014; Xu et al., 2019) in the mesopause
50 region.

51 Notably, GWs tend to dissipate rapidly in the upper atmosphere due to molecular
52 viscosity and thermal diffusion (Vadas, 2007). Thermosphere GWs that are not dissipated

53 can originate directly from the troposphere or from secondary GWs, which are generated as
54 a result of breaking of primary GWs in the mesosphere or thermosphere region (Vadas and
55 Crowley, 2010). Moreover, wave-wave, wave-mean flow, self-acceleration, and nonlinear
56 breaking also signify potential secondary wave generation mechanisms (Lund and Fritts,
57 2012; Fritts et al., 2015; Dong et al., 2020; Fritts et al., 2020; Franke and Robinson, 1999;
58 Zhou et al. 2002; Heale et al. 2020). At the same time, tunneling has been deemed as a
59 mechanism that can couple waves from tropospheric sources to the thermosphere (e.g.
60 Walterscheid and Hecht, 2003; Gavrilov and Kshevetskii;2018, Heale et al., 2021). However,
61 the lack of observations of the entire atmosphere limits our understanding of the fundamental
62 process of how the GWs propagate from the lower atmosphere to the upper atmosphere step
63 by step on the aspect of observations.

64 This paper presents a case study examining CGWs excited by Super Typhoon Chaba
65 (2016). To this end, we utilized Multi-functional Transport Satellite-1R (MTSAT-1R)
66 observations, multi-layer European Centre for Medium-range Weather Forecasts (ECMWF)
67 ERA-5 reanalysis data (Hoffmann et al., 2019; Hersbach et al., 2020), and high
68 spatio-temporal resolution double-layer airglow network (DLAN) (Xu et al., 2021)
69 observations. The CGW observations from the troposphere to the stratosphere and then to
70 the mesosphere were taken from MTSAT-1R, ERA-5, and DLAN. However, given the
71 observational limitations, the DLAN was utilized to identify the mesosphere and
72 thermosphere via the ray tracing theory. The objectives of this study were to (a) scrutinize
73 multi-layer CGW features produced by Super Typhoon Chaba (2016) from near the ground to
74 a height of 250 km, (b) to examine the entire propagation process of the CGWs excited by

typhoon from the lower atmosphere to the upper atmosphere, and (c) to provide new insights into the coupling between different atmospheric layers.

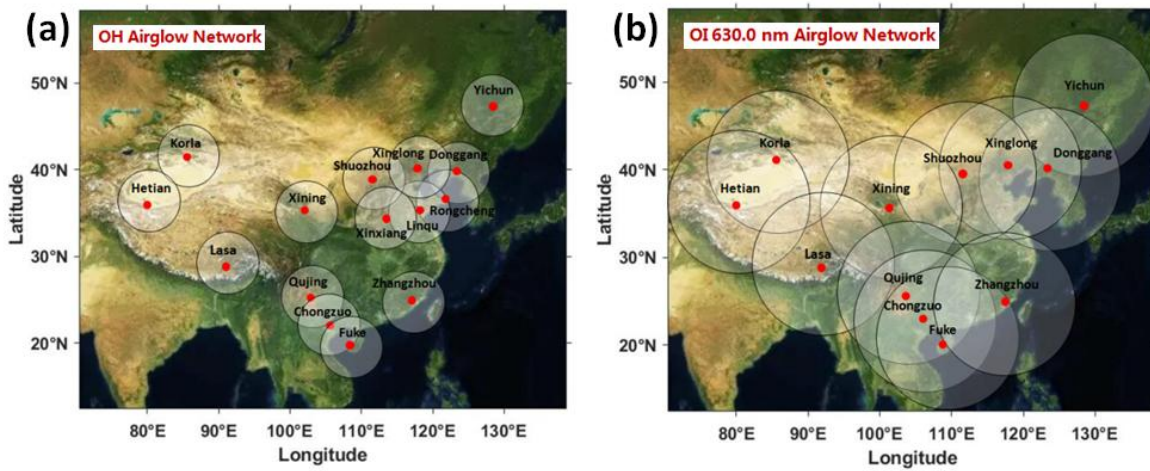
2. Data and Methods

2.1 Double layer all-sky airglow imager network data

The DLAN, including an OH layer (~87 km) and an OI 630.0 nm layer (~250 km) was established over mainland China. The research aim of DLAN is to explore the physical mechanism of vertical and horizontal propagation, as well as the evolution of atmospheric waves, triggered by severe disasters, such as typhoons, earthquakes, and tsunamis, in various middle and upper atmospheric layers. The OH airglow network comprises 15 stations, including the first no-gap OH airglow all-sky imager network located in northern China (Xu et al., 2015). The OI 630.0 nm airglow network contains 12 stations. Each imager consists of a 1024×1024 pixel back-illuminated CCD detector and a Nikon16 mm/2.8D fish-eye lens with a 180 ° field of view (FOV). The OI 630.0 nm imager is operated at the 3.0 nm band width filter with a central wavelength of 630.0 nm. Observations using airglow optical remote sensing require only a few airglow imagers to cover a wide area, although it is limited by meteorological conditions. Moreover, airglow observations can be used to monitor multi-layer GW activities. Figure 1a and 1b illustrate the OH and OI 630.0 nm network station distribution maps, respectively, in China. The OI 630.0 nm network covers nearly the entire mainland China. Furthermore, the DLAN provides an excellent solution for studying the coupling process among different atmospheric layers, especially the mesosphere and thermosphere.

Several standard procedures were applied to raw airglow images, including star

97 contamination subtraction, flat fielding to remove van Rhijin, and atmospheric extinction (Li
 98 et al., 2011). The GW structure was retrieved by taking the deviation of each processed
 99 image from a half-hour running average window image. Finally, the images were projected
 100 onto the Earth's surface using the standard star map software and the altitude of the airglow
 101 layer (Garcia et al., 1997). The altitudes of the OH and OI 630.0 nm emission layers were set
 102 as approximately 87 km and 250 km, respectively.

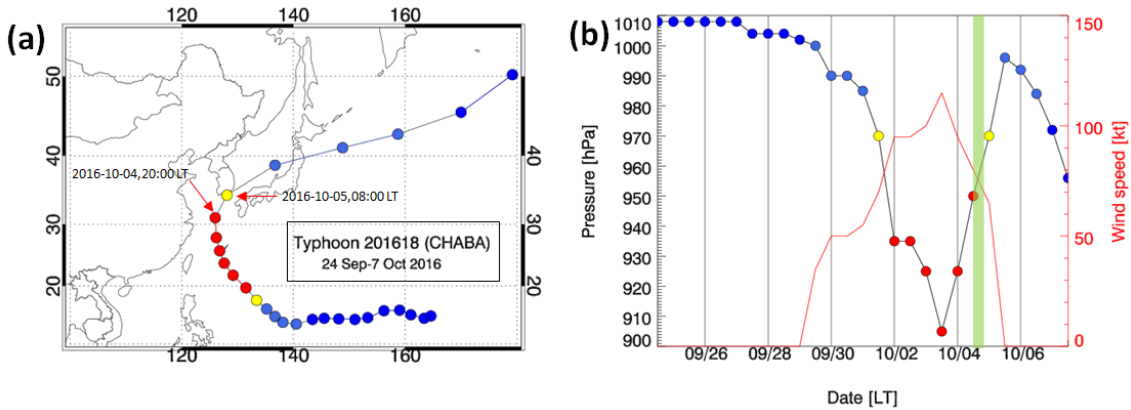


103
 104 **Figure 1. (a)** OH airglow all-sky imager network (15 stations). **(b)** Red line (630 nm) airglow all-sky
 105 imager network (12 stations). The circles on the maps give the effective observation ranges of OH and
 106 Red line airglow imagers with diameters of about 800 km and 1800 km, respectively.

107 2.2 Development of Super Typhoon Chaba

108 Super Typhoon Chaba (2016) developed in the north-western Pacific on 24 September
 109 2016 and its track is shown in Fig. 2a. Initially, it moved westward and then turned
 110 north-westward on 30 September. The central pressure in the eye of the typhoon and the
 111 maximum wind speed are shown in Fig. 2b. On 3 October 2016 at 12:00 UT, the typhoon was
 112 in the mature stage with a minimum central pressure of 905 hPa and maximum sustained
 113 winds of approximately 59 m/s. The typhoon moved northward on 3 October 2016 at 18:00
 114 UT until 4 October 2016 at 18:00 UT. The typhoon continued moving towards the northeast

115 and disappeared on 7 October 2016 at 18:00 UT. Consecutive satellite images of the typhoon
 116 from MTSAT-1R from 18:00 LT on 3 October 2016 to 00:00 LT on 5 October 2016 are shown
 117 in Fig. 3. MTSAT-1R, which belongs to the Japan Meteorological Agency, comprises a series
 118 of Geo-stationary Meteorological Satellites. MTSAT-1R is located at around 140 °E and
 119 covers East-Asia and western Pacific region. The MTSAT-1R consists of four infrared
 120 channels (IR1, IR2, IR3, and IR4) and one visible channel (VIS). The MTSAT- IR1 was used
 121 in this study. The track of the typhoon was beyond the effective FOV of the OH network and
 122 at the edge of the effective FOV of the OI 630.0 nm network, which provides an excellent
 123 example for observing the CGWs stimulated by the typhoon and studying the coupling among
 124 the atmospheric layers.



125
 126 **Figure 2.** (a) The track of Typhoon Chaba is denoted by dots from 24 September to 7 October 2016 every
 127 12 hours. (b) Central pressure of Typhoon Chaba corresponding to the tracks in (a). The maximum
 128 sustained wind speed is presented in red line. The green shadow band marks the time of ground-based
 129 airglow observation from 20:00 LT to 04:00 LT during the night of 4-5 October 2016.

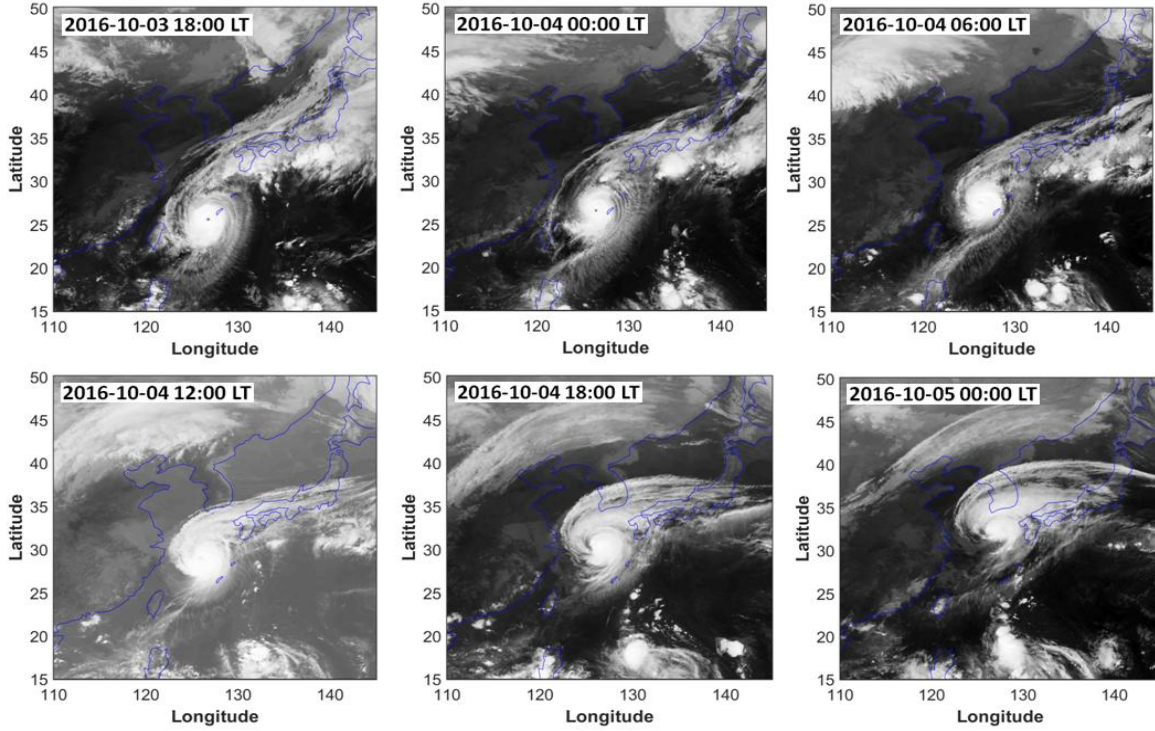


Figure 3. Consecutive satellite images of the typhoon Chaba from MTSAT-1R. The time span is from 18:00 LT on 3 October 2016 to 00:00 LT on 5 October 2016, with an interval of 6 hours.

2.3 ERA-5 reanalysis data

ERA-5 is a fifth-generation ECMWF atmospheric reanalysis that provides hourly data for many atmospheric and wave parameters. ERA-5 is produced using a four-dimensional variational data assimilation algorithm based on Integrated Forecast System (IFS), with hybrid sigma/pressure (model) levels in the vertical from 1000 hPa to 0.01 hPa (0 km to 80 km). More details of the model, data assimilation system, and observation data used to produce ERA-5 have been described by Hersbach et al. (2020). The horizontal reanalysis temperature and wind data with a pre-interpolated resolution of $0.25^\circ \times 0.25^\circ$ was used in this study. Temperature perturbations were calculated by subtracting the background with a 5×5 grid point running mean.

2.4 Ray tracing model

144 We use a ray tracing method to estimate the source location of the thermospheric
 145 secondary CGWs . This model is based on the dispersion relation that considers the
 146 molecular viscosity and thermal diffusivity (Vadas, 2007), as shown in Equation (1):

$$147 \quad m^2 = \frac{k_H^2 N^2}{\omega_{lr}^2 (1 + \delta_+ + \delta^2 / \text{Pr})} \left[1 + \frac{\nu^2}{4\omega_{lr}^2} \left(k^2 - \frac{1}{4H^2} \right)^2 \frac{(1 - \text{Pr}^{-1})^2}{(1 + \delta_+ / 2)^2} \right]^{-1} - k_H^2 - \frac{1}{4H^2}, \quad (1)$$

148 where ω_{lr} is the intrinsic frequency; $\mathbf{k}^2 = k_H^2 + m^2$, $k_H^2 = k^2 + l^2$; k , l , and m are the zonal,
 149 meridional, and vertical wave number components of the GW, respectively. The horizontal
 150 wavelength (k_H) of the CGW was obtained from the ground-based airglow observations;
 151 $N^2 = (g/T)(dT/dz + g/c_p)$ is the square of the Brunt-Väisälä frequency, where g is the
 152 gravitational acceleration, T is the background temperature, c_p is the specific heat at constant
 153 pressure, respectively; H is the scale height; $\nu = \mu/\bar{\rho}$ is the kinematic viscosity, μ is the
 154 molecular viscosity, and $\bar{\rho}$ is the background density; $\delta = \nu m / H \omega_{lr}$, $\delta_+ = \delta(1 + \text{Pr}^{-1})$, where Pr
 155 is the Prandtl number. The background temperature T and density $\bar{\rho}$ were obtained from the
 156 NRLMSISE-00 model (Picone et al., 2002).

157 The group velocity of the wave packet is formalized by Equation (2):

$$158 \quad c_{gi} = dx_i / dt = \partial \omega / \partial k_i + V_i, \quad (2)$$

159 where $V_i(u, v, w)$ is the background wind, which was obtained from the Horizontal Wind
 160 Model 14 (Drob et al., 2015), and w is the vertical wind velocity, which was neglected. Using
 161 Equations (1)-(2), we yield the ground-based (zonal, meridional, and vertical) group velocity
 162 equation as follows (Vadas and Fritts, 2005):

$$163 \quad c_{gx} = \frac{k}{\omega_{lr} B} \left[\frac{N^2 (m^2 + 1/4H^2)}{(k^2 + 1/4H^2)^2} - \frac{\nu^2}{2} (1 - \text{Pr}^{-1})^2 \left(k^2 - \frac{1}{4H^2} \right) \frac{(1 + \delta_+ + \delta^2 / \text{Pr})}{(1 + \delta_+ / 2)^2} \right] + u, \quad (3)$$

$$c_{gy} = \frac{l}{\omega_{lr}B} \left[\frac{N^2(m^2 + 1/4H^2)}{(k^2 + 1/4H^2)^2} - \frac{\nu^2}{2} (1 - \text{Pr}^{-1})^2 \left(k^2 - \frac{1}{4H^2} \right) \frac{(1 + \delta_+ + \delta^2/\text{Pr})}{(1 + \delta_+/2)^2} \right] + \nu, \quad (4)$$

$$c_{gz} = \frac{1}{\omega_{lr}B} \left\{ m \left[-\frac{k_H^2 N^2}{(k^2 + 1/4H^2)^2} - \frac{\nu^2}{2} (1 - \text{Pr}^{-1})^2 \left(k^2 - \frac{1}{4H^2} \right) \frac{(1 + \delta_+ + \delta^2/\text{Pr})}{(1 + \delta_+/2)^2} \right. \right. \\ \left. \left. + \frac{\nu^4 (1 - \text{Pr}^{-1})^4}{16H^2 \omega_{lr}^2} \frac{(k^2 - 1/4H^2)^2}{(1 + \delta_+/2)^3} - \frac{\nu^2}{\text{Pr} H^2} \right] - \frac{\nu_+ \omega_{lr}}{2H} \right\}, \quad (5)$$

$$\text{where } B = \left[1 + \frac{\delta_+}{2} + \frac{\delta^2 \nu^2}{16\omega_{lr}^2} (1 - \text{Pr}^{-1})^4 \frac{(k^2 - 1/4H^2)^2}{(1 + \delta_+/2)^3} \right], \nu_+ = \nu(1 + \text{Pr}^{-1}).$$

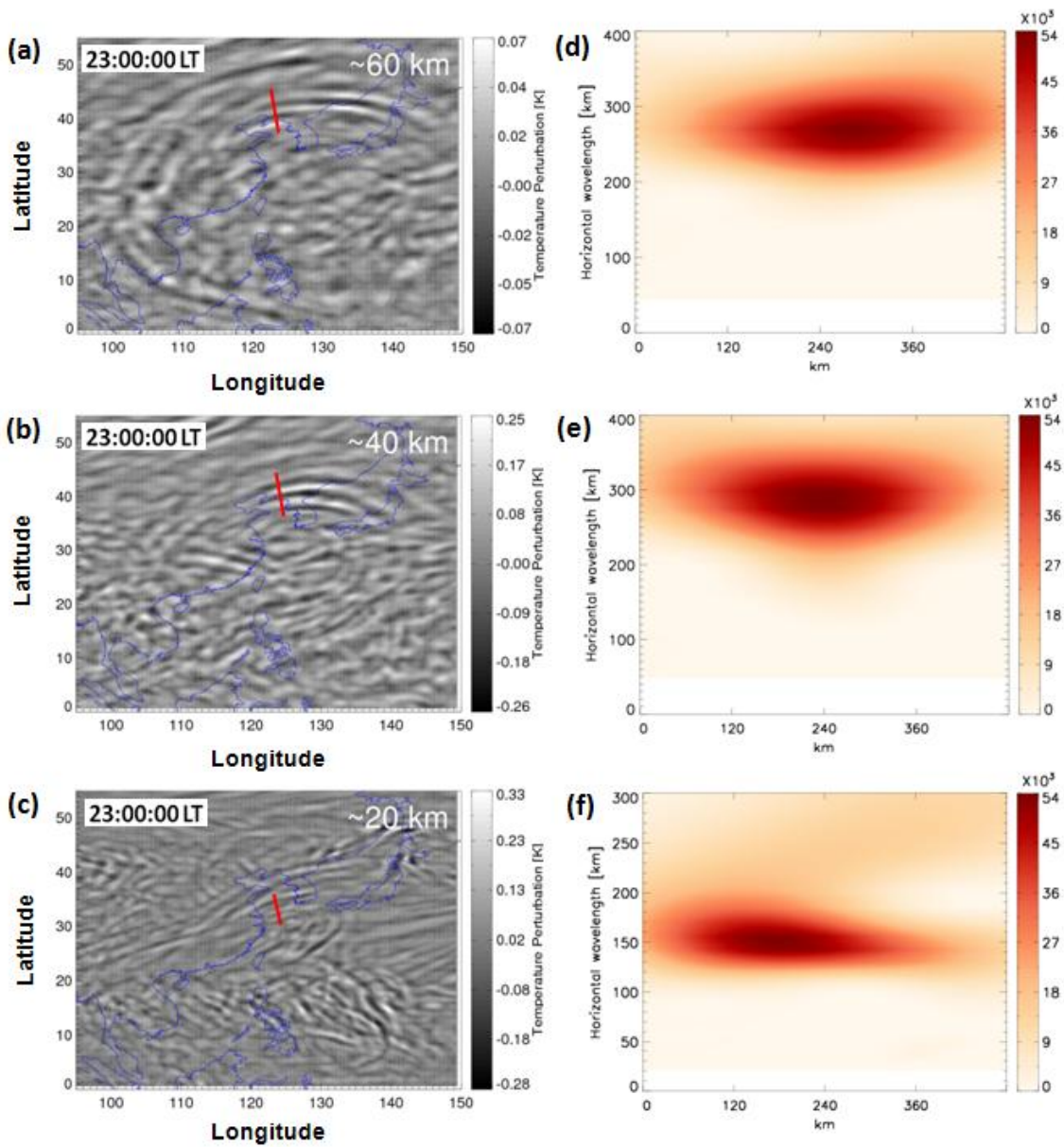
3. Results

CGWs were observed in OH and the OI 630.0 nm airglow networks during 2-5 October and 3-4 October, respectively, during super Typhoon Chaba (2016). This study focused on the CGW event that occurred on 4 October.

3.1 Propagation of typhoon induced CGWs in the stratosphere

We extracted the CGWs excited by Typhoon in the stratosphere from the ERA-5 reanalysis data. Figure 4a, 4b, and 4c show the multilayer temperature perturbations at approximately 60 km, 40 km, and 20 km at 23:00 LT, retrieved from the ERA-5 reanalysis on 4 October 2016, respectively. Figure 4d, 4e, and 4f show the corresponding wavelet analysis contours of the red line in Fig. 4a, 4b, and 4c. The temperature perturbations were calculated by subtracting the background from a 5×5 grid point running mean. The expansion area of CGW at the height of 20 km (Fig. 4c) was small, and the horizontal wavelength is approximately 150 km from Fig. 4f. Liu et al. (2014) utilized the Whole Atmosphere Community Climate model and showed that the horizontal area of the CGW expansion increases with an increase in altitude. The CGWs were present over a large area of (0°N

182 -50°N) and (100°E -150°E) at approximately 60 km. The distance of the CGWs, extending
 183 from the center of the circle ranged from 500 km (at approximately 20 km height) to 3000 km
 184 (at approximately 60 km height). The ERA-5 reanalysis data was utilized for characterizing
 185 the scale of the CGWs and indicated no small-scale fluctuation. According to the wavelet
 186 analysis of Fig. 4d and 4e, the horizontal wavelength of the northward propagating CGW at
 187 60 km (Fig. 4a) and 40 km (Fig. 4b) is approximately 265 km and 290 km, respectively.



188
 189 **Figure 4.** Temperature perturbations at (a) ~60 km, (b) ~40 km, and (c) ~20 km at 23:00LT on 4 October
 190 2016 derived from ERA-5 reanalysis. (d) The wavelet power spectrum along the red line in (a), (e) the

191 wavelet power spectrum along the red line in (b), and (f) the wavelet power spectrum along the red line in
192 (c).

193 **3.2 Propagation of typhoon induced CGWs in the mesosphere**

194 As the typhoon moved along the coast of China, CGWs were identified at ten stations
195 in the OH network. Animation 1 shows that CGWs were observed by the OH airglow
196 network during 20:00–04:00 LT (the detailed data can be downloaded from the
197 Supplementary Material). As the weather conditions in North China during the study period
198 were better than those in South China, we identified clearer wave structure at the northern
199 stations compared to those at the southern stations. Nevertheless, circular wave structures
200 were visible for brief clear weather intervals at the Zhangzhou, Qujing, and Chongzuo
201 stations. The CGWs in the mesopause region extended to 2500 km, thereby nearly covering
202 the effective FOV of the OH airglow network.

203 As long as the CGWs does not encounter the critical layer or break, the phase plane of
204 CGWs from ERA-5 reanalysis datasets can propagate to the OH airglow layer. Through the
205 propagation group velocity, we can determine the propagation time to the OH layer. A
206 single dominant horizontal wavelength is seen at the altitudes of 20 km, 40 km, and 60 km
207 in the ERA-5 reanalysis due to the limited resolution. In contrast, the horizontal scales of the
208 CGW obtained by OH airglow network are diverse, ranging from approximately 30 km to
209 300 km as the imager has much higher spatial resolution. More importantly, we found
210 some CGWs in the OH airglow layer, which are close to the CGW wavelengths at 20 km, 40
211 km, and 60 km altitudes. In order to verify whether the phase plane of the same wave is
212 propagated from the reanalysis data layer to the OH layer, we use the group velocity to

213 estimate the time when the phase plane of CGW at the altitudes of 20 km, 40 km, and 60 km
214 reaches the OH airglow layer. The times required for the CGW in the three-layer disturbance
215 diagram in Fig. 4a, 4b, and 4c reaching OH layer were approximately 28 minutes, 39
216 minutes, and 53 minutes. Therefore, the time when the phase plane of CGWs from ERA-5 at
217 the height of 60 km, 40 km, and 20 km reaches the OH airglow layer is approximately 23:28
218 LT, 23:39 LT, and 23:53 LT as shown in Fig. 5a, 5b, and 5c, respectively. We find that the
219 horizontal wavelength of CGW in the OH airglow layer (Fig. 5c) is approximately 156 km
220 from the wavelet analysis of Fig. 5f, the observed period is approximately 23 min, and the
221 horizontal speed is approximately 113 m/s, which is similar to the dominant horizontal
222 wavelength of the CGWs in the ERA-5 reanalysis at a height of 20 km. Similarly, the
223 horizontal wavelengths of CGW in the OH airglow layers (Fig. 5a and 5b) are approximately
224 270 km and 295 km from the wavelet analysis of Fig. 5d and 5e, which is similar to the
225 dominant horizontal wavelength of the CGWs in the ERA-5 reanalysis at the height of 60
226 km and 40 km. This suggests that the same CGW event can be perfectly tracked at different
227 layer altitudes, and it also suggests that the CGWs in the mesosphere come from the direct
228 excitation of the typhoon.

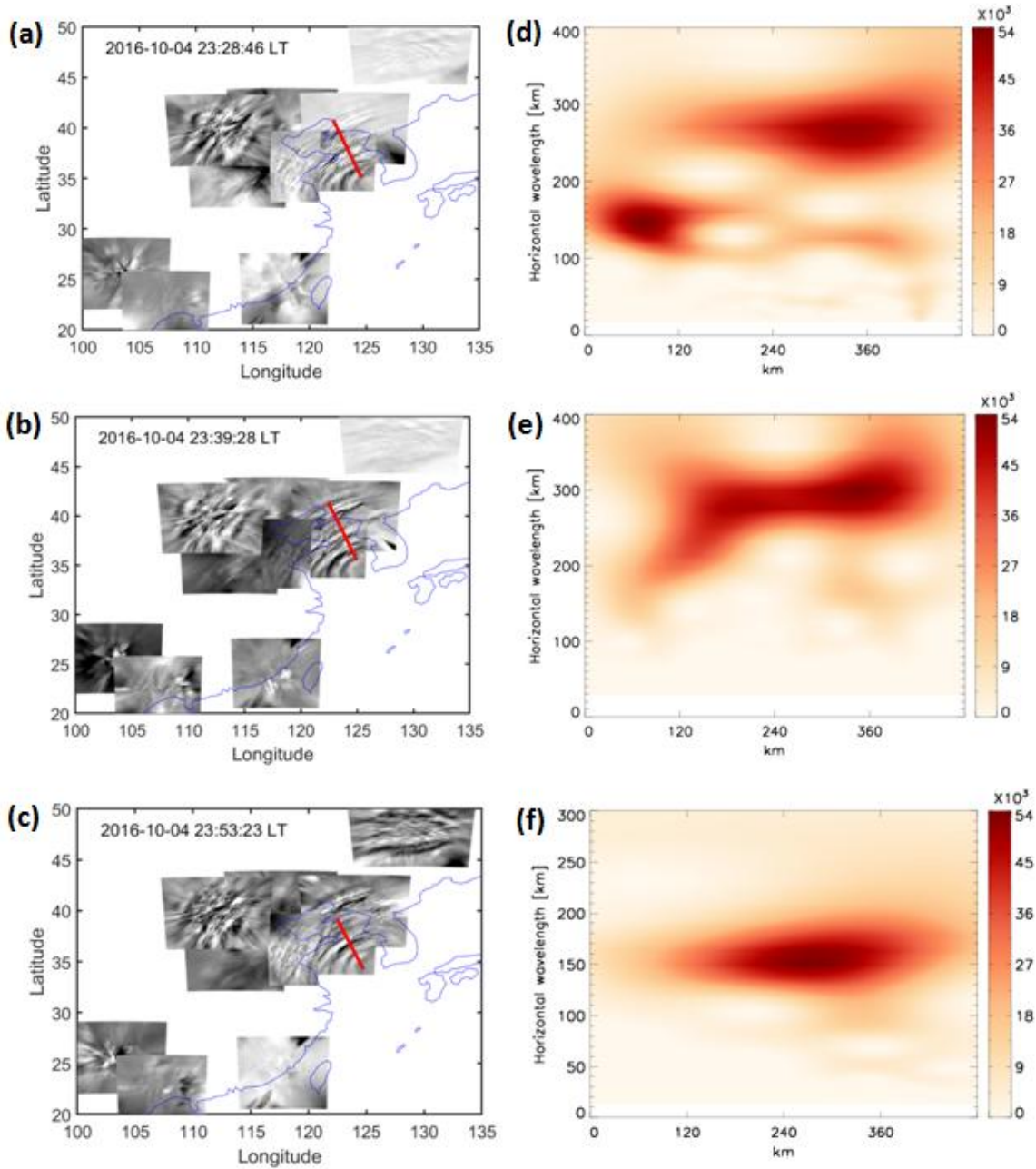


Figure 5. CGWs observed by the OH airglow imager network at (a) 23:28 LT, (b) 23:39 LT, and (c) 23:53 LT on 4 October 2016. (d) The wavelet power spectrum along the red line in (a), (e) the wavelet power spectrum along the red line in (b), and (f) the wavelet power spectrum along the red line in (c).

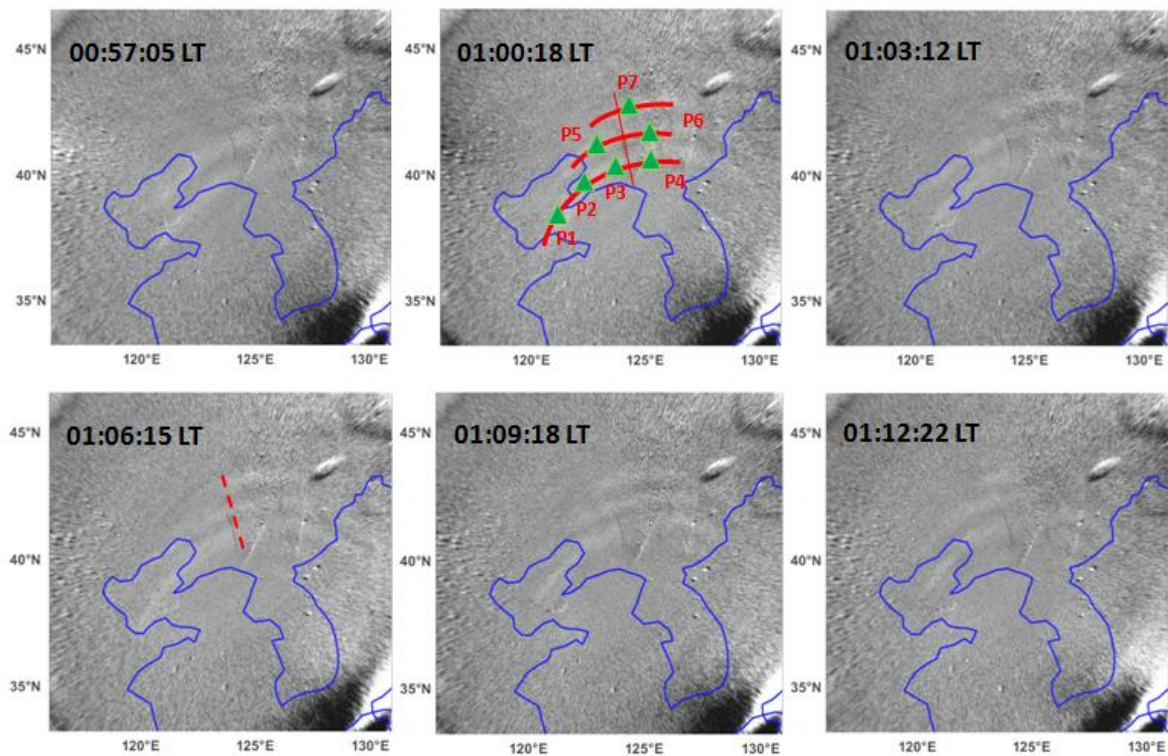
3.3 How does typhoon induced CGW propagate to the thermosphere?

Furthermore, the OI 630.0nm airglow imager network observations at the Donggang station revealed that the partial concentric ring feature lasted for 1 h from approximately 00:30 LT to 01:30 LT. The GWs generated in the troposphere can enter the thermosphere

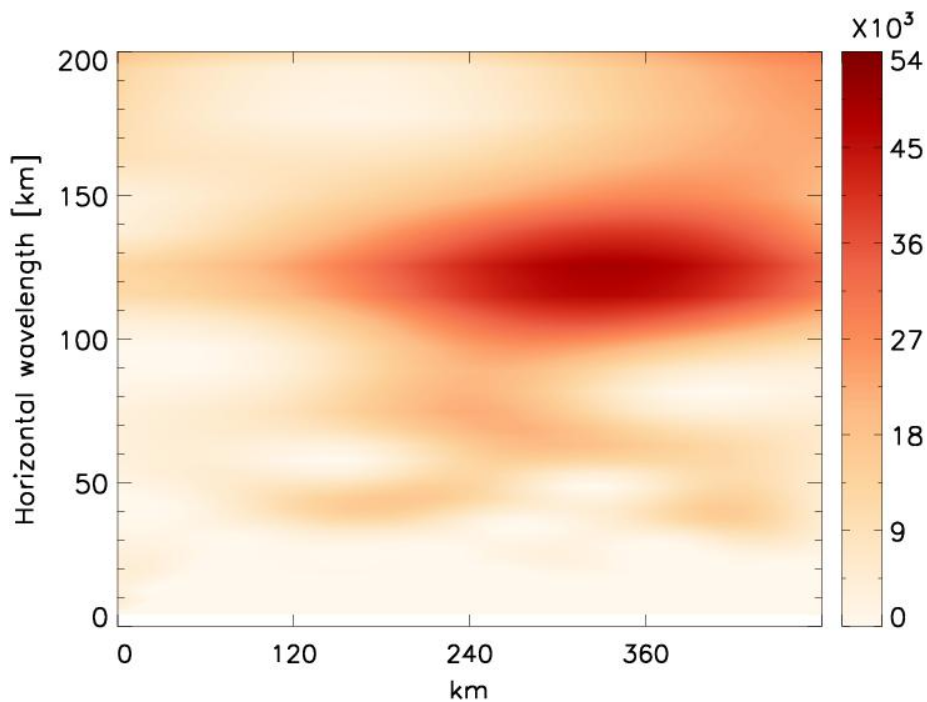
237 before breaking and/or dissipating (Vadas, 2007; Azeem et al., 2015). In contrast,
238 thermospheric GWs can originate from secondary waves generated by the breaking of GWs in
239 the mesosphere (Vadas and Fritts, 2003; Vadas and Crowley, 2010; Vadas and Azeem, 2021).

240 Figure 6 shows the time sequence of the OI 630.0nm airglow images from 00:57:05 LT
241 to 01:12:22 LT on the night of 4 October 2016. Three curved phase fronts are clearly visible.
242 The wave packet observed in the OI 630 nm airglow was quasi-monochromatic . According
243 to the wavelet analysis spectrum in Fig. 7, the horizontal wave length is approximately 120
244 km. The observation period and phase velocity are 10 min and 200 m/s, respectively. The
245 horizontal wavelength is somewhat less than the multi-scale typhoon-induced concentric
246 traveling ionosphere disturbances with a horizontal wavelength from 160 to 200 km in the
247 GNSS-TEC network as reported by Chou et al. (2017). The CGW observed in the OI 630.0
248 nm airglow having much faster phases speed and shorter period, which indicate that its
249 propagation trajectory relatively vertical. This means that they will not propagate as far
250 horizontally as the CGWs noted as dominant in the OH layer. Indeed, compared with the
251 long-distance extension of the CGWs in the mesosphere, the propagation distance of the
252 CGWs in the thermosphere was only 600 km. Numerical simulations revealed that the
253 thermosphere GWs may originate from secondary GWs generated by the breaking of primary
254 GWs in the mesosphere or thermosphere region (Vadas and Crowley, 2010). We argue that
255 the following phenomenon can represent the potential driver of this pattern. Specifically, the
256 thermospheric CGW observed by the OI 630.0 nm airglow imager was not directly
257 generated by the typhoon, but a secondary GW. To test this hypothesis, the backward
258 ray-tracing analysis was applied. In this way, we determined the source of the CGW

259 observed in the thermosphere.



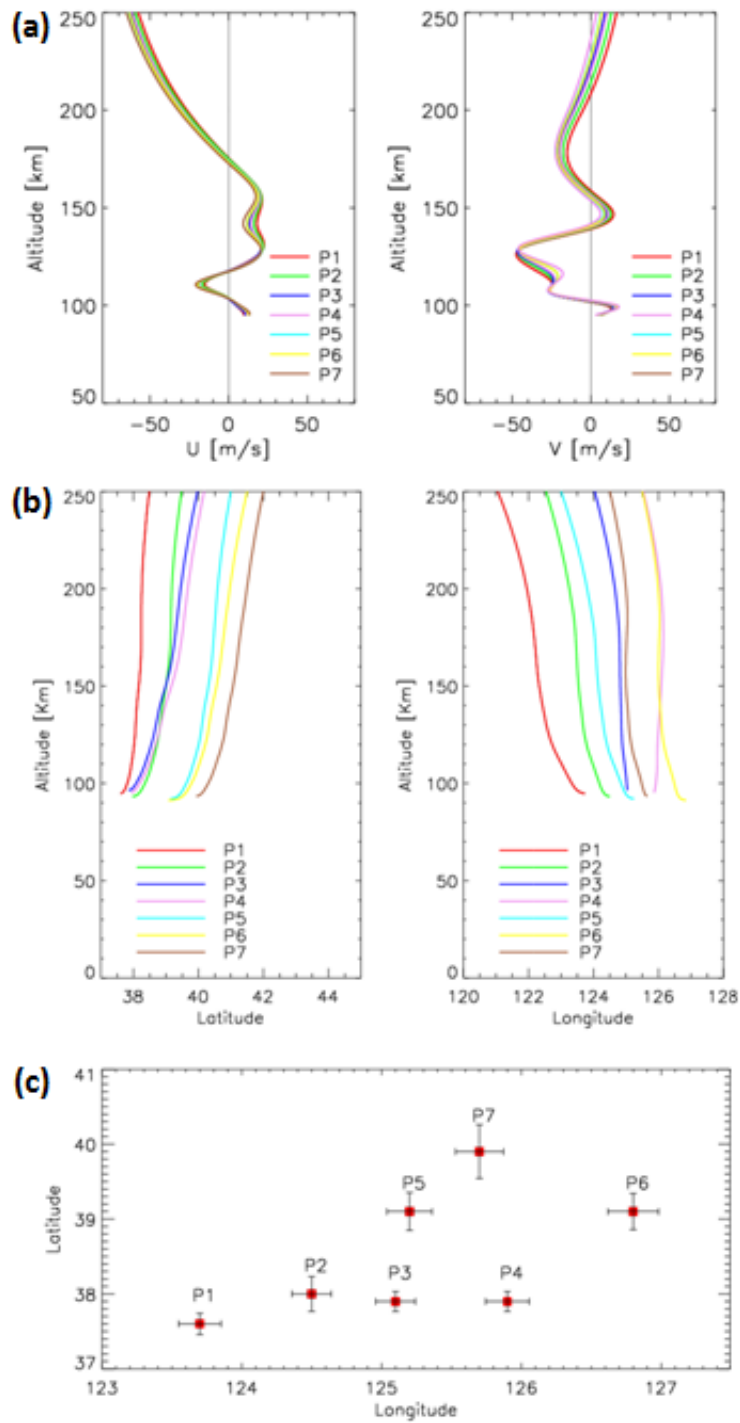
260
261 **Figure 6.** A time sequence of OI 630.0 nm airglow images observed by Donggong station during
262 00:57:05-01:12:22 LT on the night of 4 October 2016. Green triangles (P1-P7) in the red arcs are used as
263 ray tracing sampling points. The blue line in each panel represents the coastline.



264
265 **Figure 7.** The wavelet power spectrum along the red line at 01:00:18 LT in Fig. 6.

266 We sampled seven points (green triangles) on a circular wave front (red line in Fig. 6)
 267 at 01:00:18 LT as the starting point for backward ray tracing. The starting height of the
 268 backward ray tracing was 250 km. The profile of the winds used in the ray tracing is shown
 269 in Fig. 8a. The ray tracing trajectories of the seven sampling points are shown in Fig. 8b. We
 270 used the following criterion to terminate the ray tracing that the square of the vertical
 271 wavenumber should be negative. The ray tracing results of three different heights of 240 km,
 272 250 km, and 260 km are analyzed. The maximum uncertainty of horizontal change of ray
 273 tracing termination point caused by different starting heights is approximately $\pm 0.36^\circ$ in
 274 latitudinal and $\pm 0.17^\circ$ in longitudinal (see Figure 8c). Subsequently, seven backward traced
 275 trajectories took 37 minutes and terminated at the altitude of approximately 95 km thereby
 276 indicating that it met the reflection layer, which suggests that the thermospheric CGW could
 277 not have come from below 95 km according to linear theory. The thermospheric CGW
 278 could have been generated at any altitude between 95 km and the altitude of the OI 630.0 nm
 279 airglow. In other words, the CGW observed in the thermosphere was excited after
 280 approximately 00:23 LT. Meanwhile, Figure 9 presents the CGWs observed by the OH
 281 airglow network at 00:23:22 LT. We superimposed the thermospheric CGWs along with the
 282 starting ray tracing points (green triangles) reproduced from Fig. 6, and the backward ray
 283 tracing termination points (red diamonds) on the OH airglow observation images. The solid
 284 circles represent the approximate fit of CGWs, as observed by the OH airglow network. The
 285 centre of the circles is located at (31°N, 127°E), and is marked by a red dot. The dotted
 286 circle represents the approximate fitting thermospheric CGW fronts. The center of the circle
 287 is marked by a blue cross. Compared with the single-scale wave observed in the OI 630.0

288 nm layer, multi-scale CGWs are visible from OH network observations. We find that the
289 termination points of ray tracing almost fall above the mesopause region, which show clear
290 signs of dissipation and/or nonlinear processes. This suggests that the CGW observed in the
291 thermosphere did not directly originate from the typhoon, but may have emerged due to the
292 dissipation and/or nonlinear processes of typhoon-induced CGW in the mesopause region.
293 As the ray tracing mode used in this study depends on the linear theory and does not
294 consider the wave-wave and wave-mean flow interactions and tunneling, the ray tracing
295 results are limited and should be carefully taken into consideration.



296

297 **Figure8.** (a) The wind profiles along the seven ray-tracing paths. (b) The ray paths of the wave starting
 298 from the seven sampling points in Fig.6. (c) Horizontal area distribution of the terminal positions of the
 299 seven backward traced trajectories. Error bars give standard deviation for each point from the starting
 300 altitude of 240 km, 250 km, and 260km.

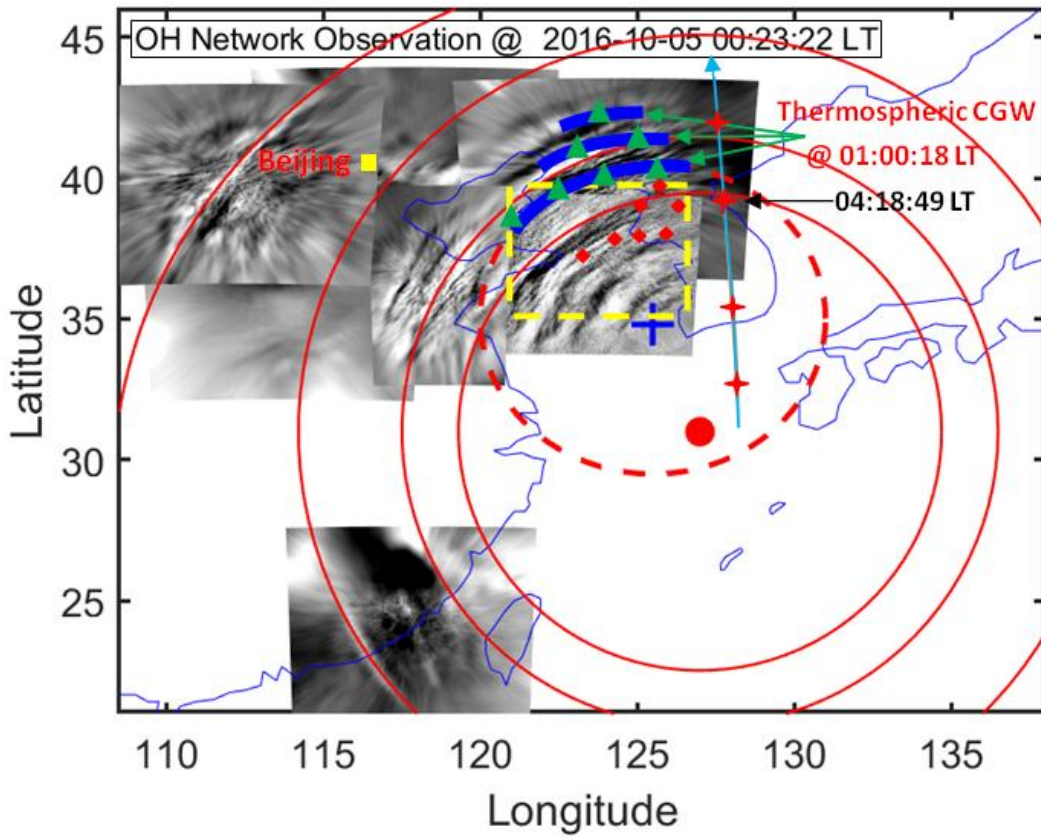
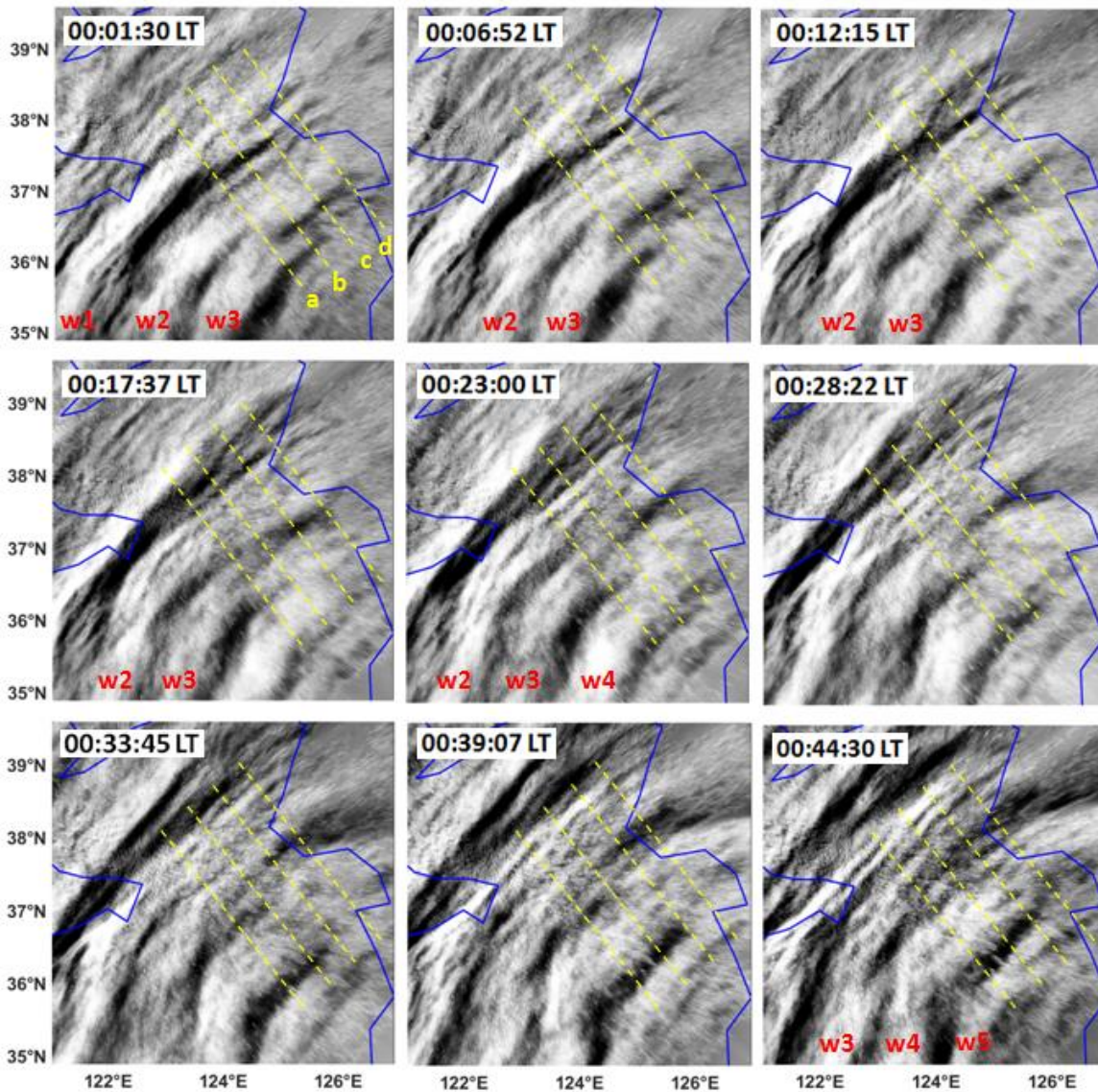


Figure 9. Two layer superimposed graph: The blue arcs represent the thermospheric CGW observed at 01:00:18 LT. The dotted circle represents the approximate fitting blue arcs. The center of the circle is marked by a blue cross. The solid circles represent the approximate fitting CGWs observed by the OH airglow network. The center of the circles is marked by a red dot. The green triangles and red diamonds represent the trace start and termination points, respectively. The red crosses represent the sounding footprints of the TIMED/SABER measurements. The yellow box marks the location of meteor radar station.

4. Discussion

We found that the strong CGWs with clear signs of dissipation and/or nonlinearity were observed by the OH airglow network both before and during the observed thermospheric CGWs on 4 October 2016. Figure 10 presents a time sequence of OH airglow images in the range marked by the yellow dotted rectangle in Fig.9. The images were

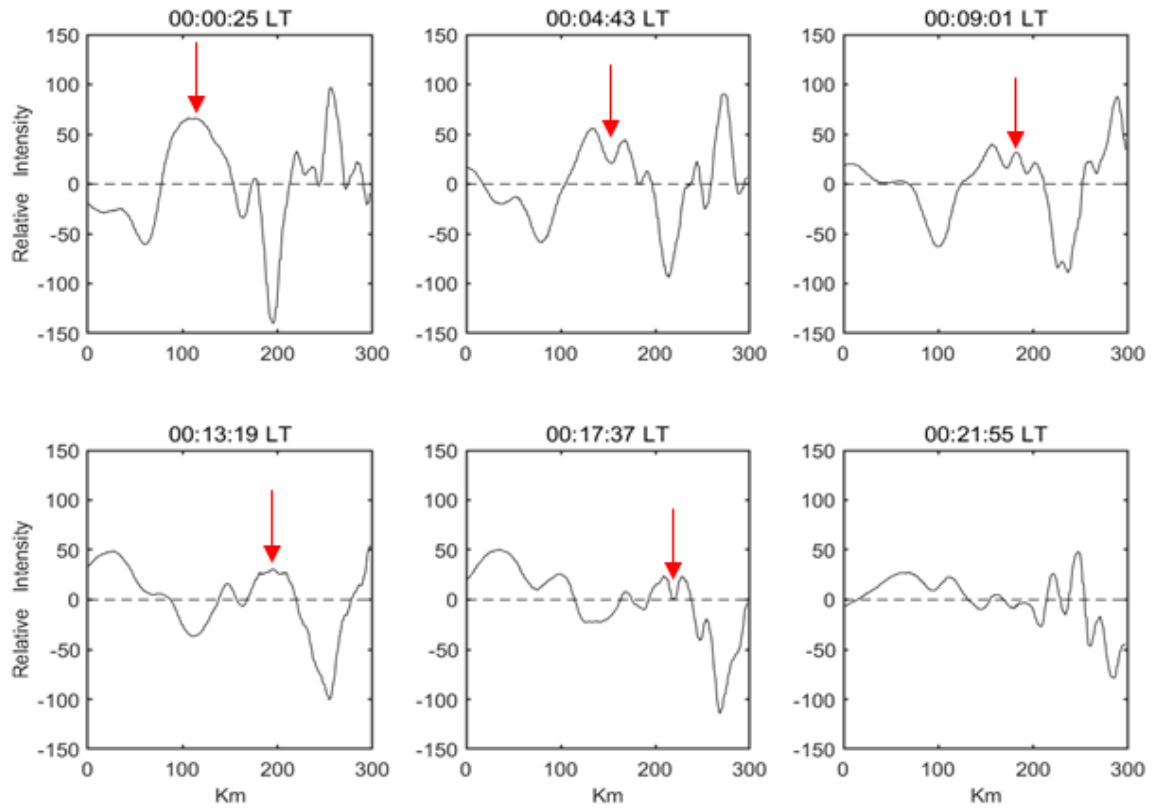
315 retrieved from the Rongcheng station from 00:01:30 to 00:44:30 LT on the night of 4
 316 October 2016. At 00:01:30 LT, three distinct curved wavefronts with the horizontal
 317 wavelength of approximately 96 km were identified. Interestingly, the wavefronts 2 and 3
 318 collided and connected in the northeast, indicating that wave-wave nonlinear interactions
 319 may have occurred.



320
 321 **Figure10.** A time sequence of OH airglow images observed by Rongcheng station during
 322 01:01:30-00:44:30 LT on the night of 4 October 2016.w1-w5 denote the wavefronts of the CGW. The
 323 blue line in each panel represents the coastline.

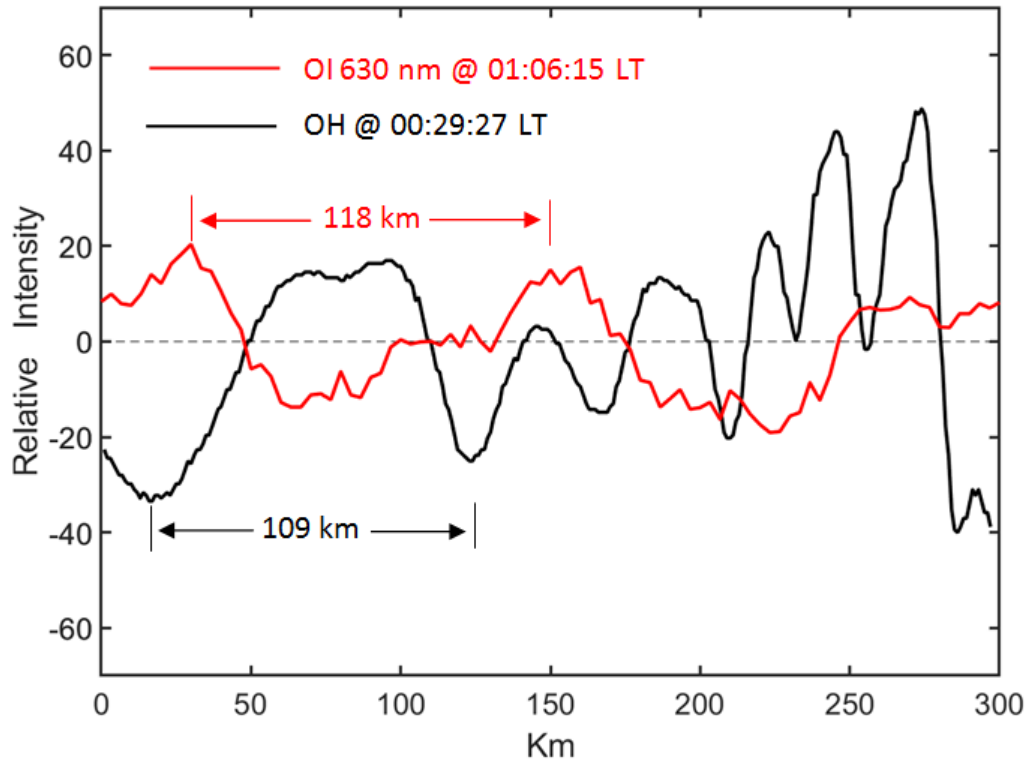
324 We elucidated the dissipation process of the CGW in detail by examining the evolution
325 process of its amplitude. Figure 11 shows the time series of the OH image slices
326 perpendicular to the wavefronts. A dominant wavelength of approximately 150 km can be
327 confirmed. As a result, we found a significant attenuation of the amplitude from 00:06:52 LT
328 to 00:17:37 LT. At 00:06:52 LT, while the relative average power is 2.3×10^3 , and the
329 amplitude decreased gradually with time. At 00:17:37 LT, the average power decreased to
330 0.15×10^3 . At the same time, we also identified the generation of approximately 110 km and
331 20-50 km small-scale waves from the larger scales, which may be caused by wave-wave
332 nonlinear interactions and/or wave breaking. We also overlay the OI 630 nm airglow relative
333 intensity variation on OH airglow variation. Figure 12 shows OH and OI 630 nm airglow
334 relative intensity variations. The OH plot is obtained at 00:29:27 LT and the OI 630 nm plot
335 is obtained at 01:06:15 LT. The time interval of 37 min is calculated by the above ray tracing
336 analysis. We found that similar scale fluctuations were obtained in the two airglow layers.
337 The horizontal wavelength of the wave obtained by OI 630 nm airglow layer is
338 approximately 118 km. The OH airglow layer has also obtained near scale fluctuations with
339 a wavelength of approximately 109 km. Therefore, the CGW seen in the thermosphere may
340 suggest come from breaking or nonlinear processes of that primary gravity wave.

341



342

343 **Figure 11.** Time series of averaged OH image slices perpendicular to the wavefronts as marked by four
 344 yellow dotted lines (a, b, c, and d) in Fig.10. The wavefronts propagate from left to right. The red arrows
 345 mark the evolution of the wavefront peak.



346

347 **Figure 12.** OH (black) and OI 630 nm (red) airglow relative intensity variations. The OH relative
 348 intensity variation is obtained as Fig. 11. The OI 630 nm relative intensity variation is from red dotted line
 349 in Fig.10 at 01:06:15 LT.

350 However, it is noted that wavepacket amplitude fluctuations can also result from the
 351 transient nature of the wavepacket. The propagation state can be studied by using the
 352 dispersion relationship with GW, but the dissipation region of the CGW lacks the real-time
 353 background temperature and wind field. In this context, TIMED/SABER can be beneficial
 354 because it occurred near the wave-dissipation region; however, the time lag was close to
 355 approximately 4 h. On this basis, we used the meteor radar wind field data from the Beijing
 356 station as auxiliary information. We further examined the dispersion relationship of GW,
 357 thereby shedding some light on the possible propagation state of dissipative waves. Figure
 358 13 presents the vertical wave number m^2 profile derived from the Beijing meteor radar wind
 359 and the temperature from the TIMED/SABER sound at 04:18:49 LT, as marked in Fig. 9.

360 The wave parameters used are from the wavefronts (w1-w5) in Fig.10. The average
361 horizontal wavelength is approximately 96 km and the average observed phase velocity is
362 approximately 90 m/s. We identified a clear duct (from 87 km to 94 km) near the peak of the
363 OH airglow layer. Note that the duct can control the horizontal propagation of CGW. This
364 implies that the CGW may indeed be dissipated. In contrast, the upper boundary of the duct
365 coincides with the height of the ray-tracing termination area mentioned above. During the
366 wave dissipation, momentum deposition occurs in the background atmosphere and can
367 produce bodyforces that stimulate the secondary GWs (Fritts et al., 2006; Chun and Kim,
368 2008; Smith et al., 2013; Heale et al., 2020). In addition, the secondary wave can be
369 generated by momentum transferred nonlinearly from the primary wave mode to harmonics
370 or subharmonics (Snively, 2017). Local momentum flux divergence associated with wave
371 breaking, vortex generation, and wave interactions can also generate secondary GWs (Fritts
372 et al., 2006).

373

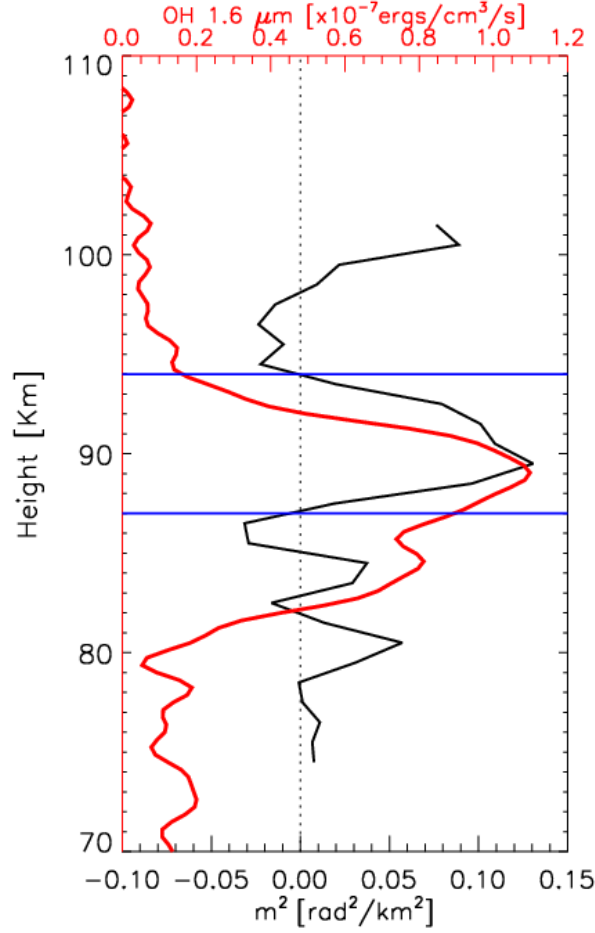


Figure 13. Vertical wave number m^2 derived from the temperature from TIMED/SABER sound at 04:18:49 LT and the meteor radar wind from Beijing station marked in Fig. 9. The red line presents the OH1.6 μm emission intensity obtained by the TIMED/SABER. The horizontal line represent the top and bottom boundaries of the duct region.

5. Summary

In this study, a double-layer airglow network (DLAN) was used to capture the CGWs over China, which were excited by the Super Typhoon Chaba (2016). We demonstrated remarkable multi-layer CGW features produced by Super Typhoon Chaba (2016) from near the ground to a height of 250 km. We applied the ERA-5 reanalysis data and MTSAT-1R observations and quantitatively described the physical mechanism of typhoon-generated

386 CGWs propagating throughout the stratosphere, mesosphere, and thermosphere.

387 Our analysis demonstrated that the CGWs in the mesopause region were excited directly
388 by the typhoon, but the CGW observed in the thermosphere may be secondary wave excited
389 by the primary CGW dissipation, breaking and/or nonlinear processes in the mesosphere,
390 rather than being directly excited by the typhoon from backward ray tracing analysis and the
391 CGWs evolution process observed by OH network. Using airglow network observations
392 combined with numerical simulation to study the generation of secondary wave in detail will
393 be carried out in the future.

394

395 ***Data availability***

396 The Double Layer Airglow Network data are available at <http://159.226.22.74/>. The ERA-5
397 reanalysis data are downloaded from the Copernicus Climate Change Service Climate Data
398 Store through <https://www.ecmwf.int/en/forecasts/datasets/reanalysis-datasets/era5>. The
399 typhoon information are provided at <http://agora.ex.nii.ac.jp/digital-typhoon/>. MTSAT-1R
400 data is accessed from <http://webgms.iis.u-tokyo.ac.jp/>.

401

402 ***Video supplement***

403 A video of detailed evolutions of CGWs excited by the Typhoon observed by OH airglow
404 observation network is provided (<https://doi.org/10.5446/55348>).

405

406 ***Author contributions***

407 J. X conceived the idea of the manuscript. Q. L. carried out the data analysis, interpretation

408 and manuscript preparation. H. L. L., X. L and W. Y. contributed to the data interpretation
409 and manuscript preparation. All authors discussed the results and commented on the
410 manuscript.

411

412 ***Competing interests***

413 The authors declare no competing interests.

414

415 ***Acknowledgements***

416 This work was supported by the National Science Foundation of China (41974179 and
417 41831073), Pandeng Program of National Space Science Center, Chinese Academy of
418 Sciences and the Strategic Priority Research Program of Chinese Academy of Sciences
419 (XDA17010301), and the Informatization Plan of Chinese Academy of Sciences
420 (CAS-WX2021PY-0101). The work was also supported by the Specialized Research Fund
421 for State Key Laboratories. We acknowledge the use of data from the Chinese Meridian
422 Project.

423

424 **References**

425 Azeem, I., Yue, J., Hoffmann, L., Miller, S. D., Straka, W. C., and Crowley, G.: Multisensor
426 profiling of a concentric gravity wave event propagating from the troposphere to the
427 ionosphere, *Geophys. Res. Lett.*, 42, 7874–7880, 2015.

428 Chun, H.-Y., and Kim, Y.-H.: Secondary waves generated by breaking of convective gravity
429 waves in the mesosphere and their influence in the wave momentum flux, *J. Geophys.*

430 Res., 113, D23107, 2008.

431 Chou, M. Y., Lin, C. C. H., Yue, J., Tsai, H. F., Sun, Y. Y., Liu, J. Y., and Chen, C. H.:
 432 Concentric traveling ionosphere disturbances triggered by Super Typhoon Meranti
 433 (2016), *Geophys. Res. Lett.*, 44,1219–1226, 2017.

434 Dong, W., Fritts, D. C., Lund, T. S.,Wieland, S. A., and Zhang, S.: Self - acceleration and
 435 instability of gravity wave packets: 2.two - dimensional packet propagation, instability
 436 dynamics, and transient flow responses, *Journal of Geophysical Research: Atmospheres*,
 437 125, 2020.

438 Drob, D. P., Emmert, J. T., Meriwether, J. W., Makela, J. J., Doornbos, E., Conde, M., et al. An
 439 update to the Horizontal Wind Model(HWM): The quiet time thermosphere, *Earth and*
 440 *Space Science*, 2, 301–319, 2015.

441 Duncombe, J.: The surprising reach of Tonga’s giant atmospheric waves, *Eos*, 103,
 442 <https://doi.org/10.1029/2022EO220050>, 2022.

443 Franke, P. M. and Robinson, W. A.: Nonlinear behavior in the propagation of atmospheric
 444 gravity waves, *J. Atmos. Sci.*, 56, 3010-3027, 1999.

445 Fritts, D. C. and Alexander, M. J.: Gravity wave dynamics and effects in the middle
 446 atmosphere, *Rev. Geophys.*,41(1), 1003, 2003.

447 Fritts, D. C., Vadas, S. L., Wan, K., and Werne J. A.: Mean and variable forcing of the middle
 448 atmosphere by gravity waves, *J. Atmos. Sol. Terr. Phys.*, 68, 247–265, 2006.

449 Fritts, D. C., B. Laughman, T. S. Lund, and Snively, J. B.: Self-acceleration and instability of

450 gravity wave packets:1. Effects of temporal localization, J. Geophys. Res. Atmos., 120,
451 8783–8803, 2015.

452 Fritts, D. C., Dong, W., Lund, T. S., Wieland, S., and Laughman, B.: Self - acceleration and
453 instability of gravity wave packets: 3.Three - dimensional packet propagation,
454 secondary gravity waves, momentum transport, and transient mean forcing in tidal winds,
455 Journal of Geophysical Research: Atmospheres, 125, 2020.

456 Garcia, F. J., Taylor, M. J., and Kelly, M. C.: Two - dimensional spectral analysis of
457 mesospheric airglow image data, Applied Optics, 36(29), 7374–7385,1997.

458 Gavrilov, N. M. and Kshevetskii, S. P.: Features of the Supersonic Gravity Wave Penetration
459 from the Earth's Surface to the Upper Atmosphere, Radio physics and Quantum
460 Electronics, 61(4), 243-252, 2018.

461 Heale, C. J., Snively, J. B., Bhatt, A. N., Hoffmann, L., Stephan, C. C., and Kendall, E. A.:
462 Multilayer observations and modeling of thunderstorm-generated gravity waves over the
463 Midwestern United States. Geophysical Research Letters, 46, 14,164–14,174.
464 <https://doi.org/10.1029/2019GL085934>, 2019.

465 Heale, C. J., Bossert, K., Vadas, S. L., Hoffmann, L., Dornbrack, A., Stober, G., et al.
466 Secondary gravity waves generated by breaking mountain waves over Europe, Journal
467 of Geophysical Research: Atmospheres,125, e2019JD031662, 2020.

468 Heale, C. J., Inchin, P. A., and Snively, J. B.: Primary Versus Secondary Gravity Wave
469 Responses at F-Region Heights Generated by a Convective Source,Journal of
470 Geophysical Research: Space Physics, <https://doi.org/10.1029/2021JA029947>, 2021.

471 Hersbach, H., Bell, B., Berrisford, P., Hirahara, S., Horányi, A., Muñoz-Sabater, J., Nicolas, J.,
 472 Peubey, C., Radu, R., Schepers, D., Simmons, A., Soci, C., Abdalla, S., Abellan, X.,
 473 Balsamo, G., Bechtold, P., Biavati, G., Bidlot, J., Bonavita, M., De Chiara, G., Dahlgren,
 474 P., Dee, D., Diamantakis, M., Dragani, R., Flemming, J., Forbes, R., Fuentes, M., Geer,
 475 A., Haimberger, L., Healy, S., Hogan, R. J., Hólm, E., Janisková, M., Keeley, S.,
 476 Laloyaux, P., Lopez, P., Lupu, C., Radnoti, G., de Rosnay, P., Rozum, I., Vamborg, F.,
 477 Villaume, S., and Thépaut, J. N.: The ERA5 global reanalysis, *Q. J. R. Meteorol. Soc.*,
 478 146(730), 1999–2049, doi:10.1002/qj.3803, 2020.

479 Hoffmann, L., Günther, G., Li, D., Stein, O., Wu, X., Griessbach, S., Heng, Y., Konopka, P.,
 480 Müller, R., Vogel, B. and Wright, J. S.: From ERA-Interim to ERA5: The considerable
 481 impact of ECMWF’s next-generation reanalysis on Lagrangian transport simulations,
 482 *Atmos. Chem. Phys.*, 19(5), 3097–3214, doi:10.5194/acp-19-3097-2019, 2019.

483 Holton, J.R.: The influence of gravity wave breaking on the general circulation of the middle
 484 atmosphere, *J. Atmos. Sci.*, 40, 2497–2507, 1983.

485 Kogure, M., Yue, J., Nakamura, T., Hoffmann, L., Vadas, S. L., Tomikawa, Y., Ejiri, M. K.,
 486 and Janches, D.: First direct observational evidence for secondary gravity waves
 487 generated by mountain waves over the Andes. *Geophysical Research Letters*, 47, 2020.

488 Li, Q., Xu, J., Yue, J., Yuan, W., and Liu, X.: Statistical characteristics of gravity wave
 489 activities observed by an OH airglow imager at Xinglong, in northern China, *Annales*
 490 *Geophysicae*, 29 (8), 1401–1410, 2011.

491 Liu, H.-L. and Vadas, S. L.: Large-scale ionospheric disturbances due to the dissipation of
 492 convectively-generated gravity waves over Brazil, *J. Geophys. Res. Sp. Phys.*, 118(5),

493 2419–2427, doi:10.1002/jgra.50244, 2013.

494 Liu, H.-L., McInerney, J. M., Santos, S., Lauritzen, P. H., Taylor, M. A., and Pedatella, N.
 495 M.: Gravity waves simulated by high-resolution Whole Atmosphere Community
 496 Climate Model, *Geophys. Res. Lett.*, 41, 9106–9112, 2014.

497 Liu, H., Ding, F., Yue, X., Zhao, B., Song, Q., Wan, W., Ning, B., Zhang, K.: Depletion and
 498 traveling ionospheric disturbances generated by two launches of China’s Long March 4B
 499 rocket. *Journal of Geophysical Research: Space Physics*, 123, 10,319–10,330, 2018.

500 Lund, T. S. and Fritts, D. C.: Numerical simulation of gravity wave breaking in the lower
 501 thermosphere, *J. Geophys. Res. Atmos.*, 117, D21105, 10.1029/2012jd017536, 2012.

502 Lund, T. S., Fritts, D. C., Wan, K., Laughman, B., and Liu, H.-L.: Numerical Simulation of
 503 Mountain Waves over the Southern Andes. Part I: Mountain Wave and Secondary Wave
 504 Character, Evolutions, and Breaking, *Journal of the Atmospheric Sciences*, 77(12),
 505 4337-4356, 2020.

506 Pfeffer, R. L. and Zarichny, J.: Acoustic-Gravity Wave Propagation from Nuclear
 507 Explosions in the Earth’s Atmosphere, *J. Atmos. Sci.* 19, 256–263, 1962.

508 Picone, J. M., Hedin, A. E., Drob, D. P., and Aikin, A. C. NRLMSISE - 00 empirical model
 509 of the atmosphere: Statistical comparisons and scientific issues, *Journal of Geophysical*
 510 *Research*, 107(A12), 1468, 2002.

511 Pierce, A.D., J. W. Posey, and Iliff, E. F.: Variation of nuclear explosion generated
 512 acoustic-gravity wave forms with burst height and with energy yield, *J. Geophys. Res.*,

513 76, 5025-5042, 1971.

514 Sentman, D. D., Wescott, E. M., Picard, R. H., Winick, J. R., Stenbaek-Nielsen, H. C.,
515 Dewan, E. M., Moudry, D. R., Sao Sabbas, F. T., Heavner, M. J., and Morrill, J.:
516 Simultaneous observations of mesospheric gravity waves and sprites generated by a
517 midwestern thunderstorm, *J. Atmos. Sol. Terr. Phys.*, 65, 537–550, 2003.

518 Smith, S. M., Vadas, S. L., Baggaley, W. J., Hernandez, G., and Baumgardner, J.: Gravity
519 wave coupling between the mesosphere and thermosphere over New Zealand, *Journal of*
520 *Geophysical Research: Space Physics*, 118, 2694–2707, 2013.

521 Smith, S. M., Setvák, M., Beletsky, Y., Baumgardner, J., and Mendillo, M.: Mesospheric
522 gravity wave momentum flux associated with a large thunderstorm complex, *Journal of*
523 *Geophysical Research: Atmospheres*, 125, e2020JD033381, 2020.

524 Snively, J. B.: Nonlinear gravity wave forcing as a source of acoustic waves in the
525 mesosphere, thermosphere, and ionosphere. *Geophysical Research Letters*, 44,
526 12,020–12,027, 2017.

527 Suzuki, S., Shiokawa, K., Otsuka, Y., Ogawa, T., Nakamura, K., and Nakamura, T.: A
528 concentric gravity wave structure in the mesospheric airglow images, *J. Geophys.*
529 *Res.*, 112, D02102, 2007.

530 Suzuki, S., Vadas, S. L., Shiokawa, K., Otsuka, Y., Kawamura, S., and Murayama, Y.:
531 Typhoon-induced concentric airglow structures in the mesopause region, *Geophys. Res.*
532 *Lett.*, 40, 5983–5987, 2013.

533 Taylor, M. J. and Hapgood, M. A.: Identification of a thunderstorm as a source of short period
 534 gravity waves in the upper atmospheric nightglow emissions, *Planet. Space Sci.*, 36,
 535 975–985, 1988.

536 Vadas, S. L., Fritts, D. C., and Alexander, M. J.: Mechanism for the generation of secondary
 537 waves in wave breaking regions, *Journal of the Atmospheric Sciences*, 60, 194–214,
 538 2003.

539 Vadas, S. L. and Fritts, D. C.: Thermospheric responses to gravity waves: Influences of
 540 increasing viscosity and thermal diffusivity, *J. Geophys. Res.*, 110, D15103,
 541 doi:10.1029/2004JD005574, 2005

542 Vadas, S. L.: Horizontal and vertical propagation and dissipation of gravity waves in the
 543 thermosphere from lower atmospheric and thermospheric sources, *Journal of*
 544 *Geophysical Research*, 112, A06305, 2007.

545 Vadas, S. L. and Crowley, G.: Sources of the traveling ionospheric disturbances observed by
 546 the ionospheric TIDDBIT sounder near Wallops Island on 30 October 2007, *Journal of*
 547 *Geophysical Research*, 115, A07324, 2010.

548 Vadas, S. L. and Liu, H.-L.: Numerical modeling of the large-scale neutral and plasma
 549 responses to the body forces created by the dissipation of gravity waves from 6 h of deep
 550 convection in Brazil, *J. Geophys. Res. Sp. Phys.*, 118(5), 2593–2617,
 551 doi:10.1002/jgra.50249, 2013.

552 Vadas, S. L. and Becker, E.: Numerical modeling of the generation of tertiary gravity waves in
 553 the mesosphere and thermosphere during strong mountain wave events over the Southern

554 Andes. Journal of Geophysical Research: Space Physics, 124,7687–7718.
 555 <https://doi.org/10.1029/2019JA026694>, 2019.

556 Vadas, S. L. and Azeem, I.: Concentric Secondary Gravity Waves in the Thermosphere and
 557 Ionosphere over the Continental United States on 25 - 26 March 2015 from Deep
 558 Convection, Journal of Geophysical Research: Space Physics,126, e2020JA028275,
 559 2021.

560 Walterscheid, R. L. and Hecht, J. H.: A reexamination of evanescent acoustic-gravity waves:
 561 Special properties and aeronomical significance, J. Geophys. Res., 108(D11), 4340,
 562 doi:10.1029/2002JD002421, 2003.

563 Xu, J., Li, Q., Yue, J., Hoffmann, L., Straka, W. C., Wang, C., Liu, M.,Yuan,W., Han, S.,
 564 Miller, S.D., Sun, L., Liu, X., Liu, W., Yang, J., and Ning, B.: Concentric gravity waves
 565 over northern China observed by an airglow imager network and satellites, J. Geophys.
 566 Res. Atmos.,120, 11,058–11,078, 2015.

567 Xu, J., Li, Q., Sun, L., Liu, X., Yuan, W., Wang, W., Yue, J., Zhang, S., Liu, W., Jiang, G., Wu,
 568 K., Gao, H., and Lai, C.: The Ground - Based Airglow Imager Network in China:
 569 Recent Observational Results, Geophysical Monograph Series, 261, 365-394, 2021.

570 Xu, S., Yue, J., Xue, X., Vadas, S. L., Miller, S. D., Azeem, I., et al. Dynamical coupling
 571 between Hurricane Matthew and the middle to upper atmosphere via gravity waves,
 572 Journal of Geophysical Research: Space Physics, 124,3589–3608, 2019.

573 Yue, J., Vadas, S. L., She, C. Y., Nakamura, T., Reising, S. C., Liu, H. L., Stamus, P., Krueger,
 574 D. A., Lyons, W., and Li, T.: Concentric gravity waves in the mesosphere generated by

575 deep convective plumes in the lower atmosphere near Fort Collins, Colorado, *J. Geophys.*
576 *Res. Atmos.*, 114(6), 1–12, doi:10.1029/2008JD011244, 2009.

577 Yue, J., Miller, S. D., Hoffmann, L., and Straka, W. C.: Stratospheric and mesospheric
578 concentric gravity waves over tropical cyclone Mahasen: Joint AIRS and VIIRS satellite
579 observations, *Journal of Atmospheric and Solar - Terrestrial Physics*, 119, 83–90, 2014.

580 Zhou, X., Holton, J. R., and Mullendore, G. L.: Forcing of secondary waves by breaking of
581 gravity waves in the mesosphere, *J. Geophys. Res. Atmos.*, 107, 2002.